



An extended core nanocoax pillar architecture for enhanced molecular detection



L.A. D'Imperio^{a,1}, A.E. Valera^{b,1}, J.R. Naughton^a, M.M. Archibald^b, J.M. Merlo^a, T.J. Connolly^b, M.J. Burns^a, T.C. Chiles^b, M.J. Naughton^{a,*}

^a Department of Physics, Boston College, Chestnut Hill, MA 02467, United States

^b Department of Biology, Boston College, Chestnut Hill, MA 02467, United States

ARTICLE INFO

Keywords:

Nanocoax
Nanofabrication
Extended-core
Biosensor
High-sensitivity
ELISA

ABSTRACT

Biosensors that incorporate nanomaterials and nanofabrication techniques enable molecular detection of chemical and biological macromolecules with a high degree of specificity and ultrasensitivity. Here, we present a novel fabrication process that yields a nanostructure capable of detecting biological macromolecules. The extended core nanocoax (ECC) structure builds on a previously reported nanocoaxial-based sensor. The fabrication of the device incorporates an extended inner pillar, with controllable extension above the annulus and into the surrounding solution. This new design eliminates structural constraints inherent in the original nanocoax architecture. We also provide results demonstrating improvement in biosensing capability. Specifically, we show the capability of the new architecture to detect the B subunit of the *Vibrio cholerae* toxin at improved sensitivity (100 pg/ml) in comparison to optical enzyme-linked immunosorbant assay (1 ng/ml) and previously reported coaxial nanostructures (2 ng/ml).

1. Introduction

Developments in on-chip, portable electrochemical biosensing tools, which are suited to point-of-care (POC) use, are limited in part by a lack of appropriate surface architectures. Signal transduction and overall sensor performance is dictated by electrode design, and as a consequence, simplistic structures, such as planar gold, may not be sufficient to maintain high sensitivity on a miniaturized platform (Grieshaber et al., 2008; Lowe, 1984; Kasemo, 1998). As such, the field of biosensing has greatly benefited from the utilization of nanomaterials and nanofabrication techniques in order to overcome these limitations (Chen et al., 2010; Roy and Gao, 2009; Brazaca et al., 2017; Wongkaew et al., 2018; Zhang et al., 2017; Zhu et al., 2015; Rizal et al., 2013). This can be understood in part by consideration of typical spatial dimensions of targets of biosensing devices, e.g. viruses, proteins, and other virulence factors, on the order of single-to-tens of nanometers (Erickson, 2009; Purohit et al., 2005). Nanoscale sensing devices improve and enable detection mechanisms by taking advantage of properties inherent to nanoscale structures, such as high surface-to-volume ratio (Liu et al., 2014), single molecule-sized pores (Feng et al., 2015), and small path lengths in nanogap electrode arrays (Shim et al., 2013;

Li et al., 2010). These and other nanoscale properties facilitate the existence and enhancements of phenomena key to biosensing, such as redox cycling (Wolfrum et al., 2016), localized electric fields (MacKay et al., 2015), and Faradaic-to-capacitive signal ratio (Morgan and Weber, 1984; Otero et al., 2016). Since these phenomena depend on the nanoscale features, small, judicious changes to these parameters can potentially result in significant improvements in device capability (Rizal et al., 2013; Arroyo-Currás et al., 2017).

A nanogap-based architecture, the nanocoax, was previously reported and shown to be able to transmit visible light (Rybczynski et al., 2007; Merlo et al., 2014), convert light to electricity (Naughton et al., 2010), and detect volatile organic compounds (Zhao et al., 2012). The nanocoax has also been used as an optrode for neurophysiology (Naughton et al., 2016). Its architecture consists of vertically oriented, concentric metal-insulator-metal layers, previously with inner and outer electrodes having the same height. The high sensitivity demonstrated in chemical (Zhao et al., 2012) and electrochemical (Rizal et al., 2013) detection indicated that the nanocoax might also hold promise for biomolecular sensing. Herein, we show how our novel fabrication, wherein the inner metal is extended above the annulus, affords a high density of biofunctionalization, greater sensitivity, and applicability for

* Corresponding author.

E-mail address: naughton@bc.edu (M.J. Naughton).

¹ These authors contributed equally to this work.

on-chip biosensing not possible in earlier iterations of the nano-coax structure (Archibald et al., 2015).

2. Materials and methods

2.1. Chemicals and reagents

Cholera toxin beta subunit antigen (CTX), ferrocenecarboxylic acid (FCA), ethanol, ethylenediaminetetraacetic acid (EDTA), and glycerol were purchased from Sigma-Aldrich (St. Louis, MO). Anti-cholera toxin subunit B polyclonal and monoclonal antibodies and alkaline phosphatase- (ALP) conjugated antibody were obtained from Abnova (Taipei, Taiwan). p-aminophenylphosphate (pAPP) was purchased from Gold Biotechnology, Inc. (St. Louis, MO). The BluePhos phosphatase substrate system was purchased from KPL (Gaithersburg, MD). Bovine serum albumin (BSA), Tween-20, phosphate buffered saline (PBS), and Tris base were obtained from Fisher Scientific (Pittsburgh, PA). Protein G was purchased from Protein Mods (Madison, WI). The Innovacoat gold nanoparticle 40 nm conjugation kit was obtained from Novus Biologicals (Littleton, CO).

Shipley 1813 photoresist, MF-319 developer, Microposit 1165, LOR-3B resist, and SU-8 were purchased from MicroChem Corp. (Westborough, MA). Transsetch-N and Cr 1020 etchants were purchased from the Transene Company, Inc. (Danvers, MA). Epon resin 828 and Epikure 3140 curing agent were obtained from Miller-Stephenson Chemical Co. Inc. (Danbury, CT). Hydrogen peroxide (27%) and ammonium hydroxide (28%) were procured from Alfa Aesar (Ward Hill, MA).

2.2. Device structure and fabrication

A schematic of the fabrication process is shown in Fig. 1. The nanostructures were fabricated on a hexagonal array of conical Si pillars with base diameter 400 nm, top diameter 200 nm, and pitch 1.3 μm (Fig. 1a). Onto these pillars was sputter-deposited a photolithographically-patterned, 10 nm-thick Ti adhesion layer followed by a 100 nm-thick Au layer. This TiAu layer forms macroscopic contact pads (not shown) and what will become the cores of the coaxes, the latter also functioning as electrochemical working electrodes (Fig. 1b). Next, annuli of the coaxial structures were formed by depositing a 150 nm thick insulating layer of Al_2O_3 by atomic layer deposition (ALD) (Fig. 1c). The Al_2O_3 was removed by wet etching with phosphoric acid (Transsetch-N) from the regions above the macroscopic gold contacts in order to enable electrical contact, though the Al_2O_3 is unchanged in the pillar regions. Next, a photolithographically-patterned 110 nm-thick Cr layer was deposited by sputtering in order to form additional macroscopic contacts (not shown) and what will become the coax shields that will function as the electrochemical counter electrodes (Fig. 1d). Positive tone photoresist S1805 was then applied by spin coating at 2000 rpm for 45 s and soft-baked for 3 min at 110 $^\circ\text{C}$ on a hotplate (Fig. 1e). The thickness of the resist in the planar regions was approximately 150 nm less than the pillar heights, and the resist formed a very thin layer on top of the pillar tops. A short 1.3 s UV flood exposure

of the resist provided a dose sufficient to expose only the region at the pillar tops. Upon development in MF-319, the pillar tops became uncovered (Fig. 1f). Etching in nitric acid / ceric ammonium nitrate (chromium etchant 1020) removed the topmost Cr region. Subsequent etching in phosphoric acid (Transsetch-N) removed the topmost Al_2O_3 region (Fig. 1g). The Cr and Al_2O_3 etch processes were repeated to further expose the inner Au electrode (Fig. 1h). This 2nd etch step results in the inner Au extending above the concentric Cr and Al_2O_3 layers, and the structure is thusly named the extended core coax (ECC). The samples were rinsed with acetone, isopropanol, and deionized H_2O before drying with N_2 gas after each photolithographic step, including producing the final structure (Fig. 1i). In order to promote adhesion, each of the Au, Cr, and Al_2O_3 deposition steps was preceded by treatment in an O_2 plasma at 400 W, 270 mTorr, and 50 SCCM O_2 flowrate for 1 min (PVA Tepla PS-210). Each sample is fabricated on a 16 mm \times 30 mm Si substrate with 7 spatially and electrically separate regions comprised of arrays of ECCs.

2.3. Characterization of nanostructures

ECC arrays were first tested for electrical integrity using a 6512 Electrometer (Keithley Instruments, Cleveland, OH). Resistance between the working and counter electrodes was measured, and any array with a resistance less than $10^6 \Omega$ was considered electrically shorted and not used for further characterization. A scanning electron microscope (SEM, JOEL 7001F, Peabody, MA) was used to collect structure images, while another SEM (JEOL JCM 6000, Peabody, MA) was used for energy-dispersive x-ray (EDX) analysis to confirm that the nanostructure was composed of Si, Au, Al_2O_3 and Cr. Initial sensing capabilities of ECCs were assessed by differential pulse voltammetry (DPV) using a potentiostat (Gamry Instruments Interface 1000, Warminster, PA). The gold core functioned as the working electrode (WE), while the chrome shield was the counter electrode (CE). An external Pt wire served as the reference electrode (RE). The current vs. applied potential of the redox species FCA was measured, where the oxidation of 1 mM FCA in PBS (pH 7.4) is used as a benchmark assay for electrochemical performance. FCA is a commonly-used redox species in electrochemical sensing, which has been highly characterized (Stepniko, 2008). A potential range from 0 mV to 500 mV was used in order to encompass the FCA redox potential at 300 mV. The potential step was 2 mV, the pulse amplitude was 50 mV, the pulse width was 50 ms, the pulse period was 100 ms, and the equilibrium time was 10 s.

2.4. On-chip enzyme-linked immunosorbant assay (ELISA)

ECC sensing arrays were biofunctionalized using a thiolated protein G diluted to 1 mg/ml in tris buffered saline (TBS). Substrates prepared as per Fig. 1 were incubated with protein G for 2 h at room temperature with rocking, after which the chips were rinsed thoroughly 3x in TBS. They were then incubated for 48 h at 4 $^\circ\text{C}$ with a primary anti-cholera toxin polyclonal antibody diluted to 1 mg/ml in 10 mM HEPES. After incubation, they were rinsed 3x in TBS with tween-20 (TBST), and blocked for 1 h at room temperature using 5% bovine serum albumin

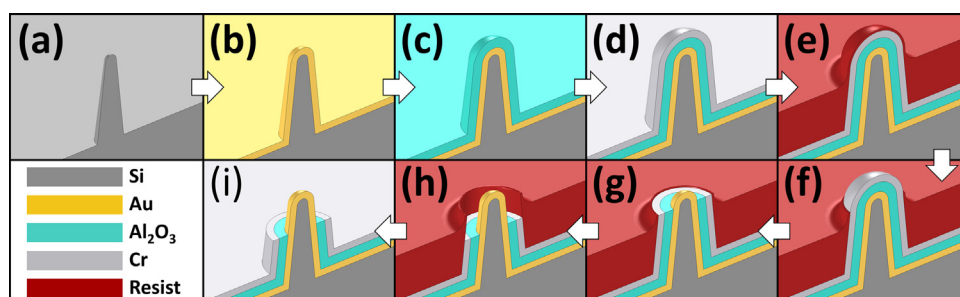


Fig. 1. Cross-sectional tilted schematic of process steps that yield coaxial nanopillar arrays with extended inner cores. (a) Si pillar array. (b) Sputtered Au preceded by 10 nm Ti adhesion layer. (c) ALD-deposited Al_2O_3 . (d) Sputtered Cr. (e) Spin coated photoresist. (f) Developed resist after a short UV exposure uncovering topmost region of pillars. (g) Wet chemical etched Cr and Al_2O_3 . (h) Further wet etched Cr and Al_2O_3 . (i) Resist dissolved and rinsed away.

(BSA) and 5% glycerol in TBST to prevent nonspecific binding to the well. A range of concentrations of CTX (100 pg/ml – 10 µg/ml) was prepared in 2% BSA/TBST, and incubated on the chip surfaces for 1 h at room temperature. The chips were again rinsed 3x with TBST. A secondary anti-cholera toxin antibody was diluted to 50 ng/ml in 2% BSA/TBST and was added to the chip surfaces for 1 h at room temperature, after which the chips were washed 3x with TBST.

Anti-mouse IgG conjugated to ALP was added at a concentration of 2.7 µg/ml for 1 h at room temperature. The chip was washed 6x with TBST and then 1 mM pAPP was added to the chip surface and incubated for 30 min in the dark at room temperature. The reaction was terminated with 20 µL of 50 mM EDTA in TBS. The 4-aminophenol (4-AP) generated in the reaction was oxidized directly on the sensing array via DPV in a potential range of –300–200 mV (to encompass the oxidation potential of 4-AP at –100 mV), with a potential step of 2 mV, a pulse amplitude of 50 mV, a pulse width of 50 ms, a sample period of 100 ms, and an equilibrium time of 10 s. Titrations of cholera toxin were analyzed by overlapping DPV signals. Nonspecific peaks were subtracted from all data points. Raw DPV signals were also subtracted to zero at –200 mV to ensure that observed peak currents were accurate.

2.5. Off-chip electrochemical ELISA

Off-chip electrochemical ELISA assessments were carried out similarly to on-chip, with the following modifications. A 96-well microtiter plate was used in place of the gold chip surface for tethering of the primary capture antibody. In order to facilitate binding to the plastic microtiter plate, the primary antibody was diluted in 0.1 M NaHCO₃ for 2 h. The plate was then blocked overnight in 5% BSA in TBST. All subsequent reagent applications (cholera toxin, secondary antibody, tertiary antibody, and enzyme substrate) and wash steps were performed in the microtiter plate as previously described. The final redox product, 4-AP, was applied to the surface of the ECC for electrochemical measurement. DPV settings were as previously described for 4-AP redox.

2.6. Optical ELISA

Optical ELISAs were performed identically to the off-chip ELISA, with the exception that for the last step, the BluePhos phosphatase system replaced pAPP as the reaction substrate. Absorbance was measured spectroscopically at $\lambda = 600$ nm on a SpectraMax M5 (Molecular Devices, Sunnyvale, CA).

3. Results

3.1. Fabrication

SEM images of the structure at different steps of the fabrication process are shown in Fig. 2a–f. Fig. 2g shows the final ECC structure at x5 lower magnification than in Fig. 2f, while Fig. 2h shows a x150 lower magnification view of the final structure, with a wide enough field of view to show the leads to the 250 µm-diameter sensing region.

Our work was motivated by an earlier generation nanocoax device that was capable of CTX detection via electrochemical ELISA using an off-chip strategy (Archibald et al., 2015). In that work, all steps of the ELISA were performed in a standard 96-well microtiter plate, with only the electrochemical detection carried out on the nanocoax array. The arrangement of the nanoscale gap between the working and counter electrodes precluded liquid exchange, preventing fully on-chip detection (i.e. the tethering of all sensing components to a chip surface).

To overcome this limitation, the gold core of the nanocoax reported herein is extended above the chrome shield, resulting in the ECC as described above. This retains the benefits of the coaxial architecture, with its nanoscale proximity of the WE and CE and also allows for facile reagent exchange. It also creates an unobstructed WE gold surface,

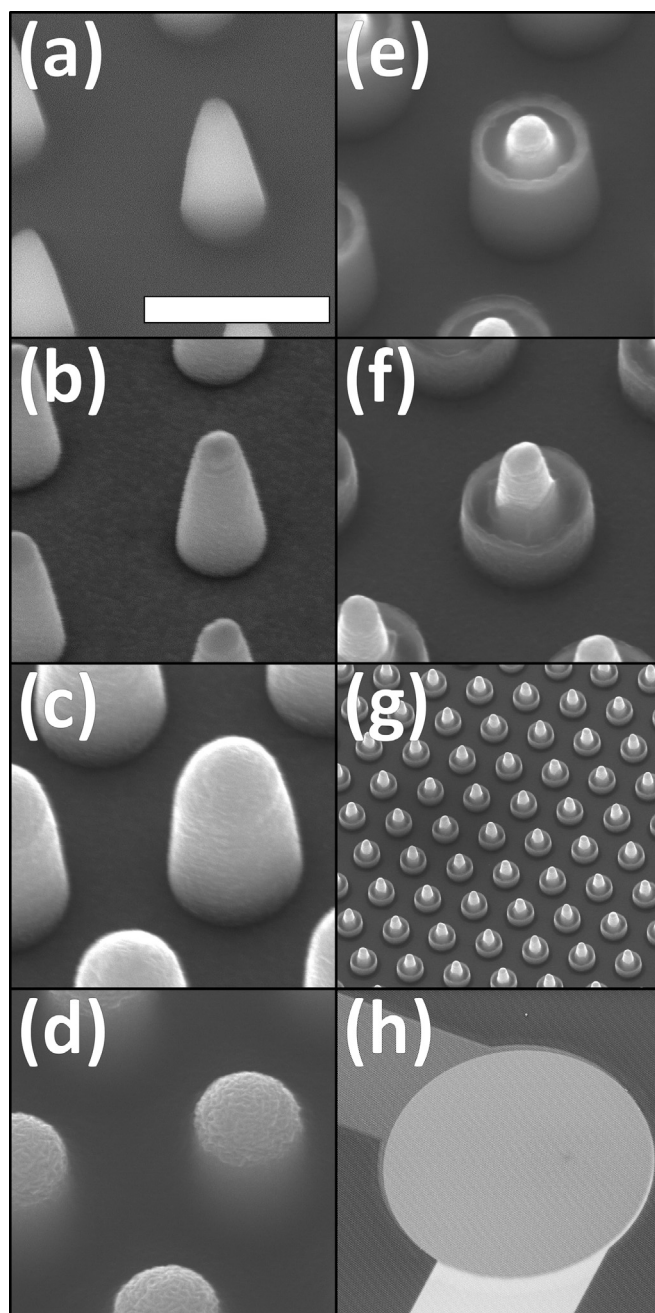


Fig. 2. SEMs of different stages and magnifications during the fabrication process (30° tilt). (a) Si pillar array. (b) Sputtered Au preceded by 10 nm Ti adhesion layer. (c) After ALD Al₂O₃ and sputtered Cr. (d) Spin coated, exposed and developed photoresist uncovering topmost region of pillars. (e) After wet chemical etched Cr and Al₂O₃ with resist removed. (f–h) After 2nd wet etched Cr and Al₂O₃ with resist removed at different magnifications. Scale bar in (a) is 1 µm for images (a–f), 5 µm for (g), and 150 µm (h).

which introduces the possibility for biofunctionalization.

In developing the ECC architecture, a set of fabrication parameters was identified to provide superior performance in response to FCA oxidation relative to that in a previously reported nanocoaxial sensor (Rizal et al., 2013). One focus was the size of the annulus gap, which is the dielectric layer between the WE and CE. In order to function as a nanogap electrode and allow for high sensitivity, as gauged by the current response during electrochemical oxidation, the WE and CE must be in nanoscale proximity. Previous non-ECC iterations fabricated with sub-100 nm annulus gaps experienced inconsistent liquid exchange in

washing steps, and also experienced relatively lower manufacturing yield, possibly associated with electrical shorting caused by the size of the gap. Because of a necessity to be able to wash the chips between reagent incubation steps, as well as a desire for higher manufacturing yield, an annulus gap of 150 nm was used for all ECC chips. Al₂O₃ thicknesses above 150 nm were not used in order to maintain the nanogap electrode proximity. The 100 nm thickness of the Au and Cr layers was chosen to be thick enough for sufficient conductivity for these electrodes, while thin enough to maintain the aspect ratio in the pillar geometry.

We further explored a number of modifications at several steps in fabrication parameters in order to develop the final protocol shown in Figs. 1 and 2. For example, we explored fabricating devices on several different-shaped silicon arrays (Supplementary information Fig. S1), and identified a core electrode shape that provided both a high level of reproducibility and a high manufacturing yield. We next focused on modifications to the etching steps involved in forming the extended core (Fig. 2e and f). The effects of all changes were gauged by FCA redox performance and compared against the non-ECC devices and planar Au electrodes, in order to maximize sensitivity. Computer simulations performed in COMSOL Multiphysics were used to inform design changes. As an example, Fig. 3a and b show the normalized electric field distribution corresponding to different shield heights for the nanocoax. The greater penetration of the Au WE into the high electric field region suggested that extended core configurations would facilitate higher current response and device sensitivity, which was corroborated by FCA (1 mM) redox data (Fig. 3c). Based on these findings, we finalized our ECC architecture as a chip containing 7 individually-addressed sensing arrays, each array comprised of ~30,000 nanocoaxes connected in parallel. The measured electrochemical current in response to 1 mM FCA oxidation of these arrays demonstrated a high level of experimental reproducibility *i.e.*, ~9% variation in peak current over 9 consecutive measurements (Supplementary information Fig. S2a). This consistency was not achievable on previous nanocoaxes, which exhibited a drop in peak FCA oxidation current in each subsequent run until finally stabilizing at a significantly lower current (likely because of liquid exchange issues) (Supplementary information Fig. S2b). Variation in peak current between independently fabricated ECCs is larger than that in repeated measurements on an individual sensing region (Supplementary information, Fig. S2c). It should be noted that this variation does not affect an individual region's viability and that the important metric for detection is a region's response to 4-AP redox, which falls in the nA range. Thus, to overcome any potential issues resulting from the variability of individually fabricated chips, a baseline of 1 μ A current in response to FCA oxidation was established to be the minimum acceptable performance. This corresponds to ~20 μ A/mm² current density, which is also comparable to that used for the non-ECC (Archibald et al., 2015).

Fig. 4a shows a comparison of the peak current density achieved on 3 sensing platforms: a simple planar electrode, the non-ECC, and the ECC nanocoax. It is apparent from the results that the ECC represents a significant improvement over its predecessor, as well as over simpler to fabricate architectures lacking a nanogap.

3.2. ECCs as biosensors

3.2.1. Off-chip ELISA

After fabrication optimization and confirmation of electrochemical function, ECCs were evaluated for their biosensing capabilities and compared to the non-ECC version. Non-ECCs had previously been used to detect CTX in an off-chip setup; in other words, all ELISA steps were performed in a 96 well microtiter plate and only the final redox product was applied to the chip surface for detection. As a baseline for comparison of the non-ECC and the ECC as biosensors, an off-chip electrochemical ELISA was performed. CTX was chosen as the biomarker of interest due to its clinical relevance and overall stability. The off-chip

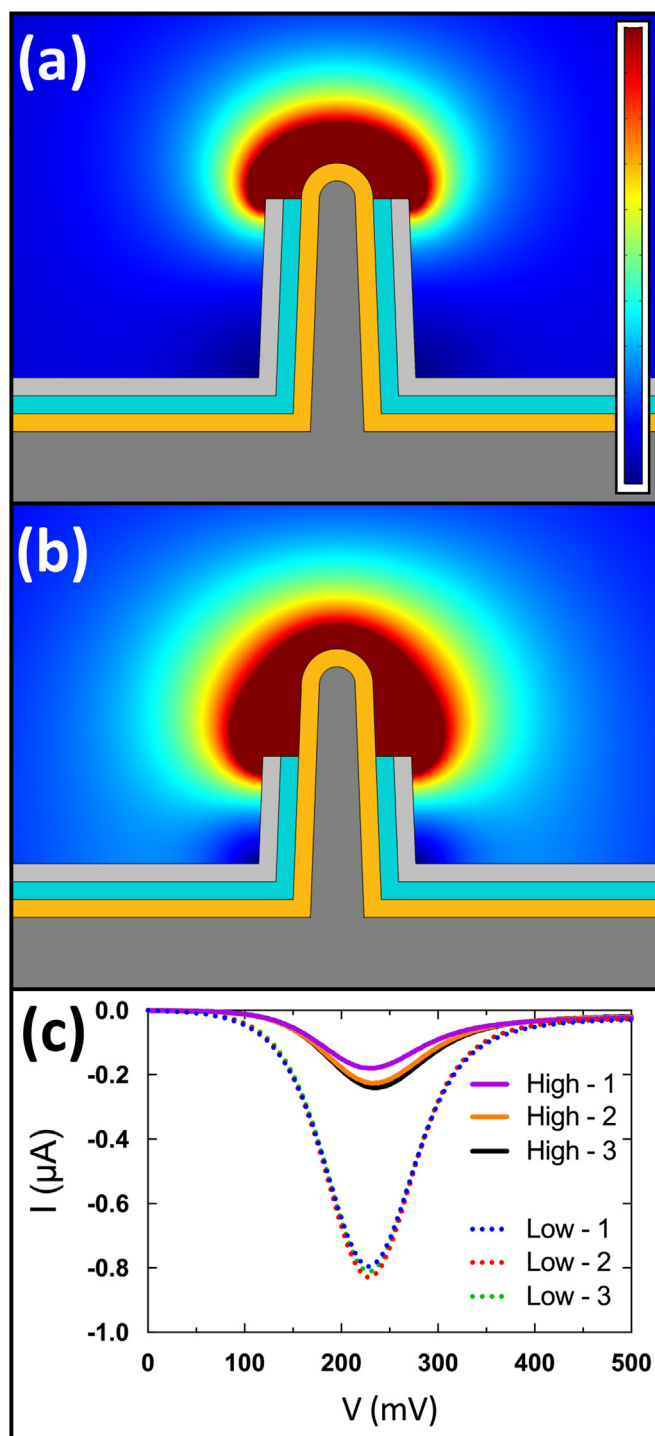


Fig. 3. Cross-sectional view of geometry with overlaid simulated electric field norm for 1 V applied to coaxial terminals for the (a) high shield configuration and (b) the low shield configuration (simulated in COMSOL). Inset linear color scale ranges from 0 V/m (blue) to 2×10^5 V/m (red) and inset white scale bar is 1 μ m. (c) DPV current response of oxidizing 1 mM FCA comparing the two shield configurations (3 runs each) shows that the electric field distribution of the low shield results in a 4x relative increase in the current response, a metric of sensitivity. (For interpretation of the references to color in this figure legend, the reader is referred to the web version of this article).

ELISA was performed identically on the ECC and non-ECC, and in turn was identical to a standard optical ELISA, with the exception of the readout. For the electrochemical ELISA, pAPP was added as the enzymatic substrate as opposed to Bluephos for the optical readout. The

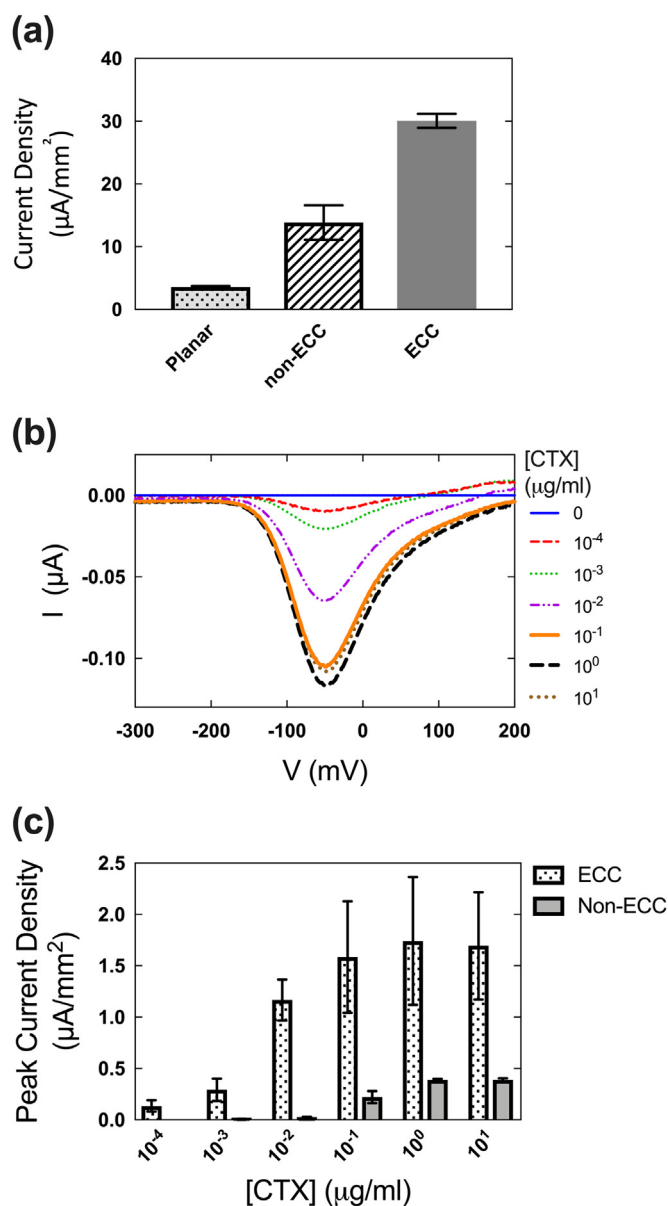


Fig. 4. Electrochemical comparisons of the ECC vs. planar and non-ECC architectures. (a) The average current density resulting from the detection of the oxidation of 1 mM FCA is shown for a representative ECC array, a non-ECC array and a planar gold electrode. (b) Current as a function of applied potential for electrochemical ELISAs performed off-chip for CTX concentrations ranging from 100 pg/ml to 10 $\mu\text{g}/\text{ml}$, analyzed on the ECC. All measurements were made on the same ECC array to minimize variability. (c) Peak ELISA current density as a function of CTX concentration, measured on an ECC chip and a non-ECC chip, showing both increased response and lower limit-of-detection for the ECC configuration. All error bars represent the standard deviation of 3 trials.

current response of the ECC off-chip ELISA (Fig. 4b) was superior to that of the non-ECC (100 pg/ml vs. 2 ng/ml). The ECC demonstrated a linear sensitivity range between 0.1 and 100 ng/ml. An optical ELISA utilizing the same antibodies was capable of detecting as low as 1 ng/ml of CTX, meaning the ECC outperformed this clinical standard. When current density was taken into account, the ECC vastly outperformed the non-ECC, as the ECC sensing area was significantly smaller than that of the non-ECC (0.049 mm^2 vs. 1.8 mm^2) (Fig. 4c).

3.2.2. On-chip biofunctionalization

Protein G was utilized to facilitate antibody tethering to the ECC surface. This is a bacterially-derived protein with a high affinity and

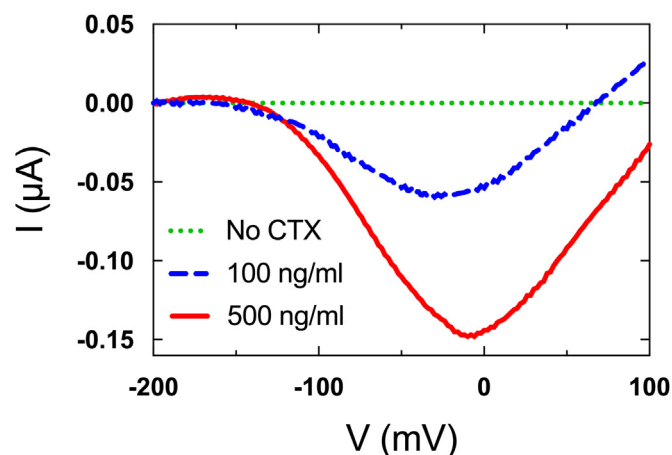


Fig. 5. Current response as a function of applied voltage for ECCs in on-chip detection of CTX, using protein G to tether antibodies to the sensor surface. Shown are one trial for each condition of 500 ng/ml (red, solid) and 100 ng/ml (blue, dash) concentrations alongside a control sample with no CTX (green). Each trial was performed on a separate array on the same ECC chip. Data were subtracted to a baseline at -200 mV to better show peak current. Deviations from -100 mV for the 4-AP oxidation peak are likely due to the use of a pseudo-reference electrode. (For interpretation of the references to color in this figure legend, the reader is referred to the web version of this article).

specificity for the Fc region of IgGs (Björck and Kronvall, 1984; Sjöbring et al., 1991). For the purposes herein, it was modified with a thiol group, in order to also facilitate binding with a gold surface (Pensa et al., 2012). We first obtained visual (SEM) proof-of-concept of tethering by conjugating a 40 nm gold nanoparticle to our tertiary ELISA antibody (Supplementary information Fig. S3). These results confirmed biofunctionalization of the gold core of the ECC with an IgG. We next sought to complete a full on-chip ELISA on the ECC. Our results demonstrate on-chip detection of CTX by an ECC functionalized with protein G (Fig. 5).

4. Discussion

The ECC device was developed in response to architectural constraints that prevented adequate fluid exchange within the annulus of the nanocoax. In order to enable on-chip biofunctionalization, we fabricated the ECC to have a gold core that extended outside of the shield, which would be highly available to reagents, and allow for easy washing. The resulting ECC demonstrated a significant increase in sensitivity to FCA redox compared to prior generations of nanocoax, and to a planar control electrode.

The increase in current density, which nanocoax architectures exhibit over planar electrodes, may be explained by the phenomenon of redox cycling. Redox cycling occurs between nanogap electrodes, where a species is oxidized at the WE, then reduced at the proximate CE, where it can then rapidly diffuse back to the proximate WE to be oxidized again (Wolfrum et al., 2016; White and McKelvey, 2018). Improvement in signal can be obtained by decreasing the size of the annulus gap that, in turn, may allow for faster redox cycling (Rizal et al., 2013), though eliminating electrical shorting for sub-100 nm annuli needs to be addressed. A simple planar gold electrode with millimeter-to-centimeter scale distances between electrodes cannot match the sensitivity because this cycling does not occur, and thus sensitivity is dominated by the rate of reagent diffusion to the electrode surface.

As both nanocoaxial architectures contain nanogap electrodes, the increase in current density that the ECC exhibits over the non-ECC may be explained by the ease of liquid exchange. In order to interact with the WE it will be necessary for liquid reagents to diffuse into the

annulus gap of the non-extended core nanocoax. In actuality, high surface tension and morphology-induced hydrophobicity caused by the size of the gap hindered this, and additionally made it difficult to wash the chip surface for further reagent application. By contrast, the ECC WE extends into the solution and so it may be easier for FCA and 4-AP molecules to move from the bulk solution to the electrode surface to be oxidized.

The ECC demonstrated a greater sensitivity toward CTX than an optical ELISA, with the ECC detecting at 100 pg/ml in an off-chip format vs. 1 ng/ml for optical. However, the ECC holds the potential to be functionalized, allowing for all detection steps to be performed on a miniaturized platform, making it a more portable and lower-cost alternative to an optical ELISA. This is because the nanocoax device achieves its sensitivity while requiring significantly less analyte (as little as 10^{-5} as much) compared to macroscopic optical ELISAs, lowering the cost per assay. Based on this, we suggest the ECC is a promising architecture for further development toward fully on-chip biomarker detection. We have established preliminary on-chip detection, but future experiments, including measuring a broader range of CTX concentrations with the on-chip configuration, are needed to fully validate the ECC architecture as a clinically-viable candidate for a POC diagnostic tool.

As it stands, however, the current device is competitive with nanogap devices reported in literature (Table 1). Once full on-chip capabilities are confirmed, the ECC will represent a promising alternative to simpler, planar nanogap-style electrodes because of the increase in functionalizable surface area resulting from the number of coaxes in each array, and their 3D architecture. We also believe that the protein G biofunctionalization assay represents a much simpler method of antibody tethering than those frequently used in the literature, such as silane or cysteamine functionalization.

Another important feature of the ECC is its amenability to repeated use. The non-ECC chips exhibited signal degradation over the course of several uses. Conversely, ECC chips maintained signal integrity with less than 10% change in response over 9 runs, suggesting that the ECCs are relatively stable structures. Taken together, these data confirm that the ECC represents a significant improvement over the non-ECC architecture. However, while we have demonstrated the ECC's capability of consistent repeated use for measurements that are solely chemical detection, e.g., in FCA and 4-AP tests, it is important to note that each ECC sensing region is currently used for a single on-chip detection assay. The regeneration of biosensing devices has shown promise for enabling repeated use, thereby potentially reducing diagnostic costs, although only a third of reported electrochemical biosensor studies meet previously-reported criteria (Goode et al., 2015). To forgo this problem, we made 7 separate submillimeter size sensing regions on an individual sample, thereby achieving the same end-of-line benefit as sample regeneration. Furthermore, the number of sensing regions could be increased beyond 7, as each region is less than 0.1% of the active sample area.

Lastly, in order for the benefits of such a biosensing device to be relevant to diagnostic applications, it must be affordable in order to

meet the demands of the resource-limited areas where diseases like cholera are most prevalent. Several aspects of the ECC facilitate this criterion. The photolithographic processes involved in patterning each layer are amenable to large wafer-scale throughput. The chemical wet etching processes are high-throughput, while the chemicals are inexpensive and can be reused for extended periods, given the nanoscopic amount of material etched. Multiple sensing regions on a given chip, as previously discussed, can further reduce a sample's cost per test. Si pillar arrays used herein can be easily and inexpensively replicated in polymer (e.g. SU8) by nanoimprint lithography (NIL). As an electrochemical sensor, detection using an ECC is performed with equipment that is less expensive than that used in standard optical ELISA. As such, further reduction of electrochemical equipment cost is possible by incorporation of inexpensive microcontroller units such as Arduino.

5. Conclusions

We have demonstrated that an extended core nanocoax is capable of sensitive and repeatable detection of a target antigen in an off-chip setup with a detection limit of 100 pg/ml, with preliminary data suggesting it possesses utility as an on-chip electrochemical biosensor. We have demonstrated that the ECC architecture is a viable and promising alternative to the non-ECC nanocoax architecture. Future directions may include examining more coax core pillar shapes to further improve device sensitivity. We have demonstrated that the ECC fabrication is comprised of processes and chemicals that are suitable for high-throughput, and future works will target these advantages in order to further decrease the cost per sample. Future works will also include the fabrication of a more sophisticated chip housing that incorporates microfluidics and a portable analysis system in order to enable the ECC's use for POC detection of infectious disease biomarkers, offering the potential to meet the diagnostic needs of resource-limited areas.

Acknowledgements

The authors thank Steve Shepard in the Boston College Integrated Science Clean Room Facility for advice and assistance in device fabrication, Richard Pijar for assistance making and repairing electronic components for experiments, and Roger J. Fleischmann for technical support.

Declaration of interest statement

All authors certify that they have no affiliations with or involvement in any organization or entity with any financial interest, or non-financial interest in the subject matter or materials discussed in this manuscript.

Author contributions

A.E. Valera planned the study, performed experiments related to biological detection, analyzed results and co-wrote the original draft of

Table 1

A comparison of nanogap-based protein detection platforms.

Citation	Biomarker	Lowest concentration detected (ng/ml)	Recognition scheme	Transduction
<i>Current device</i>	<i>Cholera toxin subunit B</i>	<i>0.1 (off chip) 100 (on chip)</i>	<i>Thiolated protein G antibody tethering</i>	<i>DPV</i>
(Singh et al., 2010)	C reactive protein	0.1	Cysteamine SAM	EIS
(Hsueh and Lin, 2016)	Cardiac-troponin T	0.1	Silane functionalization	CV
(Ilyas et al., 2012)	Epidermal growth factor receptor	50	Immobilized aptamer	Impedance
(Whited et al., 2012)	HE4 Biomarker	1.5 (standalone) 0.1 (mixed)	Cysteamine SAM	EIS
(Kim et al., 2009)	Prostate specific antigen	0.0001	Protein G antibody tethering	Electrical
(Carlo and Lee, 2003)	Laminin	10	Silane functionalization	Capacitive

the manuscript. L.A. D'Imperio optimized ECC design, fabricated all devices, performed quality control, and co-wrote the original draft of the manuscript. J.R. Naughton established the ECC fabrication methodology. M.M. Archibald developed the initial off-chip ELISA methodology. J.M. Merlo provided scientific supervision in the fabrication of devices. T.J. Connolly and M.J. Burns provided scientific supervision as experts in biology and physics. T.C. Chiles co-supervised experiments. M.J. Naughton conceptualized the ECC design, provided scientific supervision and laboratory equipment for analysis, and co-conceived of the original nanocoaxial architecture. All authors also reviewed and edited the manuscript.

Appendix A. Supplementary material

Supplementary data associated with this article can be found in the online version at doi:10.1016/j.bios.2019.03.045.

References

- Archibald, M.M., Rizal, B., Connolly, T., Burns, M.J., Naughton, M.J., Chiles, T.C., 2015. A nanocoaxial-based electrochemical sensor for the detection of cholera toxin. *Biosens. Bioelectron.* 74, 406–410. <https://doi.org/10.1016/j.bios.2015.06.069>.
- Arroyo-Currás, N., Scida, K., Ploense, K.L., Kippin, T.E., Plaxco, K.W., 2017. High surface area electrodes generated via electrochemical roughening improve the signaling of electrochemical aptamer-based biosensors. *Anal. Chem.* 89, 12185–12191. <https://doi.org/10.1021/acs.analchem.7b02830>.
- Björck, L., Kronvall, G., 1984. Purification and some properties of streptococcal protein G, a novel IgG-binding reagent. *J. Immunol.* 133, 969–974. <https://doi.org/10.1385/1-59259-076-4:281>.
- Brazaca, L.C., Ribovski, L., Janegitz, B.C., Zucolotto, V., 2017. Nanostructured materials and nanoparticles for point of care (POC) medical biosensors. *Med. Biosens. Point Care Appl.* 229–254. <https://doi.org/10.1016/B978-0-08-100072-4.00010-1>.
- Carlo, C.D., and Lee, L.P., 2003. Nanogap-based dielectric immunosensing. In: *Transducers '03. Proceedings of the 12th International Conference on Solid-State Sensors, Actuators and Microsystems. Digest of Technical Papers (Cat. No. 03TH8664)*, pp. 1180–1183 vol.2. <http://dx.doi.org/10.1109/SENSOR.2003.1216982>.
- Chen, X., Guo, Z., Yang, G.M., Li, J., Li, M.Q., Liu, J.H., Huang, X.J., 2010. Electrical nanogap devices for biosensing. *Mater. Today* 13, 28–41. [https://doi.org/10.1016/S1369-7021\(10\)70201-7](https://doi.org/10.1016/S1369-7021(10)70201-7).
- Erickson, H.P., 2009. Size and shape of protein molecules at the nanometer level determined by sedimentation, gel filtration, and electron microscopy. *Biol. Proced. Online* 11, 32–51. <https://doi.org/10.1007/s12575-009-9008-x>.
- Feng, Y., Zhang, Y., Ying, C., Wang, D., Du, C., 2015. Nanopore-based fourth-generation DNA sequencing technology. *Genom. Proteom. Bioinforma.* 13, 4–16. <https://doi.org/10.1016/j.gpb.2015.01.009>.
- Goode, J.A., Rushworth, J.V.H., Millner, P.A., 2015. Biosensor regeneration: a review of common techniques and outcomes. *Langmuir* 31, 6267–6276. <https://doi.org/10.1021/la503533g>.
- Grieshaber, D., MacKenzie, R., Vörös, J., Reimhult, E., 2008. Electrochemical biosensors - Sensor principles and architectures. *Sensors*. <https://doi.org/10.3390/s8031400>.
- Hsueh, H.-T., Lin, C.-T., 2016. An incremental double-layer capacitance of a planar nanogap and its application in cardiac-troponin T detection. *Biosens. Bioelectron.* 79, 636–643. <https://doi.org/10.1016/j.bios.2015.12.105>.
- Ilyas, A., Asghar, W., Allen, P.B., Duhon, H., Ellington, A.D., Iqbal, S.M., 2012. Electrical detection of cancer biomarker using aptamers with nanogap break-junctions. *Nanotechnology* 23, 275502. <https://doi.org/10.1088/0957-4484/23/27/275502>.
- Kasemo, B., 1998. Biological surface science. *Curr. Opin. Solid State Mater. Sci.* 3, 451–459. [https://doi.org/10.1016/S1359-0286\(98\)80006-5](https://doi.org/10.1016/S1359-0286(98)80006-5).
- Kim, S.K., Cho, H., Park, H.-J., Kwon, D., Lee, J.M., Chung, B.H., 2009. Nanogap biosensors for electrical and label-free detection of biomolecular interactions. *Nanotechnology* 20, 455502. <https://doi.org/10.1088/0957-4484/20/45/455502>.
- Li, T., Hu, W., Zhu, D., 2010. Nanogap electrodes. *Adv. Mater.* 22, 286–300. <https://doi.org/10.1002/adma.200900864>.
- Liu, S., Wang, Z., Wang, F., Yu, B., Zhang, T., 2014. High surface area mesoporous CuO: a high-performance electrocatalyst for non-enzymatic glucose biosensing. *RSC Adv.* 4, 33327–33331. <https://doi.org/10.1039/c4ra04700a>.
- Lowe, C.R., 1984. *Biosensors. Trends Biotechnol.* 2, 59–65. [https://doi.org/10.1016/0167-7799\(84\)90011-8](https://doi.org/10.1016/0167-7799(84)90011-8).
- MacKay, S., Hermansen, P., Wishart, D., Chen, J., 2015. Simulations of interdigitated electrode interactions with gold nanoparticles for impedance-based biosensing applications. *Sensors (Switz.)* 15, 22192–22208. <https://doi.org/10.3390/s150922192>.
- Merlo, J.M., Ye, F., Rizal, B., Burns, M.J., Naughton, M.J., 2014. Near-field observation of light propagation in nanocoax waveguides. *Opt. Express* 22, 14148. <https://doi.org/10.1364/OE.22.014148>.
- Morgan, D.M., Weber, S.G., 1984. Noise and signal-to-noise ratio in electrochemical detectors. *Anal. Chem.* 56, 2560–2567. <https://doi.org/10.1021/ac00277a065>.
- Naughton, J.R., Connolly, T., Varela, J.A., Lundberg, J., Burns, M.J., Chiles, T.C., Christianson, J.P., Naughton, M.J., 2016. Shielded coaxial optrode arrays for neurophysiology. *Front. Neurosci.* 10, 1–10. <https://doi.org/10.3389/fnins.2016.00252>.
- Naughton, M.J., Kempa, K., Ren, Z.F., Gao, Y., Rybczynski, J., Argenti, N., Gao, W., Wang, Y., Peng, Y., Naughton, J.R., McMahon, G., Paudel, T., Lan, Y.C., Burns, M.J., Shepard, A., Clary, M., Ballif, C., Haug, F.J., Söderström, T., Cubero, O., Eminian, C., 2010. Efficient nanocoax-based solar cells. *Phys. Status Solidi - Rapid Res. Lett.* 4, 181–183. <https://doi.org/10.1002/pssr.201004154>.
- Otero, T.F., Martinez, J.G., Asaka, K., 2016. Faradaic and capacitive components of the CNT electrochemical responses. *Front. Mater.* 3, 1–11. <https://doi.org/10.3389/fmats.2016.00003>.
- Pensa, E., Cortés, E., Corthey, G., Carro, P., Vericat, C., Fonticelli, M.H., Benítez, G., Rubert, A.A., Salvarezza, R.C., 2012. The chemistry of the sulfur-gold interface: In search of a unified model. *Acc. Chem. Res.* 45, 1183–1192. <https://doi.org/10.1021/ar200260p>.
- Purohit, P.K., Inamdar, M.M., Grayson, P.D., Squires, T.M., Kondev, J., Phillips, R., 2005. Forces during bacteriophage DNA packaging and ejection. *Biophys. J.* 88, 851–866. <https://doi.org/10.1529/biophysj.104.047134>.
- Rizal, B., Archibald, M.M., Connolly, T., Shepard, S., Burns, M.J., Chiles, T.C., Naughton, M.J., 2013. Nanocoax-based electrochemical sensor. *Anal. Chem.* 85, 10040–10044. <https://doi.org/10.1021/ac402441x>.
- Roy, S., Gao, Z., 2009. Nanostructure-based electrical biosensors. *Nano Today* 4, 318–334. <https://doi.org/10.1016/j.nantod.2009.06.003>.
- Rybczynski, J., Kempa, K., Herczynski, A., Wang, Y., Naughton, M.J., Ren, Z.F., Huang, Z.P., Cai, D., Giersig, M., 2007. Subwavelength waveguide for visible light. *Appl. Phys. Lett.* 90. <https://doi.org/10.1063/1.2430400>.
- Shim, J.S., Rust, M.J., Ahn, C.H., 2013. A large area nano-gap interdigitated electrode array on a polymer substrate as a disposable nano-biosensor. *J. Microchem. Microeng.* 23. <https://doi.org/10.1088/0960-1317/23/3/035002>.
- Singh, K.V., Whited, A.M., Ragineni, Y., Barrett, T.W., King, J., Solanki, R., 2010. 3D nanogap interdigitated electrode array biosensors. *Anal. Bioanal. Chem.* 397, 1493–1502. <https://doi.org/10.1007/s00216-010-3682-z>.
- Sjöbring, U., Björck, L., Kastern, W., 1991. Streptococcal protein G. *J. Biol. Chem.* 266, 399–405. <https://doi.org/10.1099/mic.0.039578-0>.
- Stepnik, P., 2008. *Ferrocenes: Ligands, Materials and Biomolecules*. Wiley.
- White, H.S., McKelvey, K., 2018. Redox cycling in nanogap electrochemical cells. *Curr. Opin. Electrochem.* 7, 48–53. <https://doi.org/10.1016/j.coelec.2017.10.021>.
- Whited, A.M., Singh, K.V., Evans, D., Solanki, R., 2012. An electronic sensor for detection of early-stage biomarker/s for ovarian cancer. *BioNanoSci* 2, 161–170. <https://doi.org/10.1007/s12668-012-0049-2>.
- Wolfrum, B., Kätelhön, E., Yakushenko, A., Krause, K.J., Adly, N., Hüske, M., Rinklin, P., 2016. Nanoscale electrochemical sensor arrays: redox cycling amplification in dual-electrode systems. *Acc. Chem. Res.* 49, 2031–2040. <https://doi.org/10.1021/acs.accounts.6b00333>.
- Wongkaew, N., Simsek, M., Griesche, C., Baumner, A.J., 2018. Functional nanomaterials and nanostructures enhancing electrochemical biosensors and lab-on-a-chip performances: recent progress, applications, and future perspective. *Chem. Rev.* <https://doi.org/10.1021/acs.chemrev.8b00172>.
- Zhang, S., Geryak, R., Geldmeier, J., Kim, S., Tsukruk, V.V., 2017. Synthesis, assembly, and applications of hybrid nanostructures for biosensing. *Chem. Rev.* 117, 12942–13038. <https://doi.org/10.1021/acs.chemrev.7b00088>.
- Zhao, H., Rizal, B., McMahon, G., Wang, H., Dhakal, P., Kirkpatrick, T., Ren, Z., Chiles, T.C., Naughton, M.J., Cai, D., 2012. Ultrasensitive chemical detection using a nanocoax sensor. *ACS Nano* 6, 3171–3178. <https://doi.org/10.1021/nn205036e>.
- Zhu, C., Yang, G., Li, H., Du, D., Lin, Y., 2015. Electrochemical sensors and biosensors based on nanomaterials and nanostructures. *Anal. Chem.* 87, 230–249. <https://doi.org/10.1021/ac5039863>.

SUPPLEMENTARY MATERIALS DOCUMENT

An extended core nanocoax pillar architecture for enhanced molecular detection

L.A. D'Imperio*, A.E. Valera*, J.R. Naughton, M.M. Archibald, J.M. Merlo, T.J. Connolly, M.J. Burns, T.C. Chiles, and M.J. Naughton

* These authors contributed equally to this work.

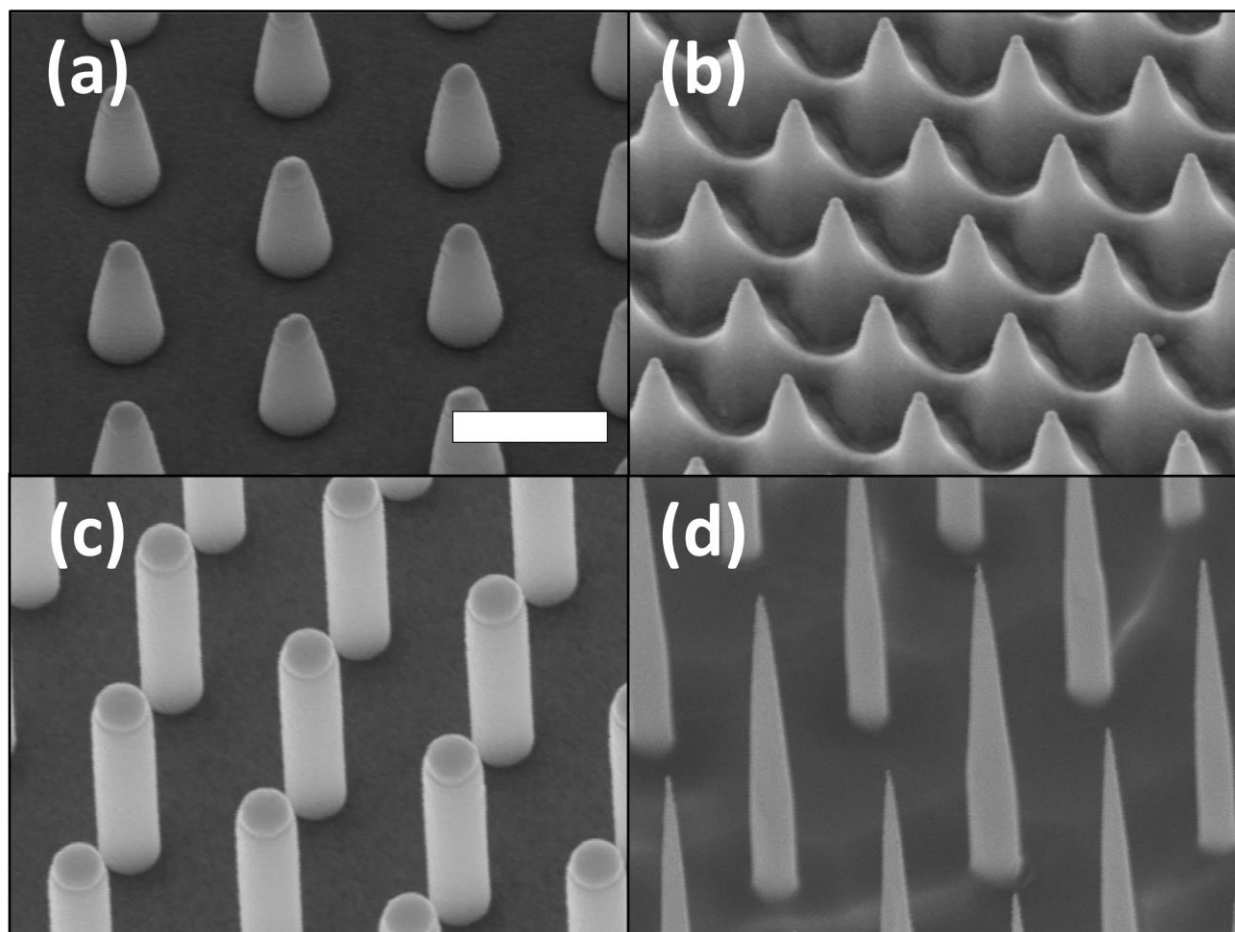
Abstract

Biosensors that incorporate nanomaterials and nanofabrication techniques enable molecular detection of chemical and biological macromolecules with a high degree of specificity and ultrasensitivity. Here, we present a novel fabrication process that yields a nanostructure capable of detecting biological macromolecules. The extended core nanocoax structure builds on a previously reported nanocoaxial-based sensor. The fabrication of the device incorporates an extended inner pillar, with controllable extension above the annulus and into the surrounding solution. This new design eliminates structural constraints inherent in the original nanocoax architecture. We also provide results demonstrating improvement in biosensing capability. Specifically, we show the capability of the new architecture to detect the B subunit of the *Vibrio cholerae* toxin at improved sensitivity in comparison to optical enzyme-linked immunosorbant assay and the previously reported coaxial nanostructures.

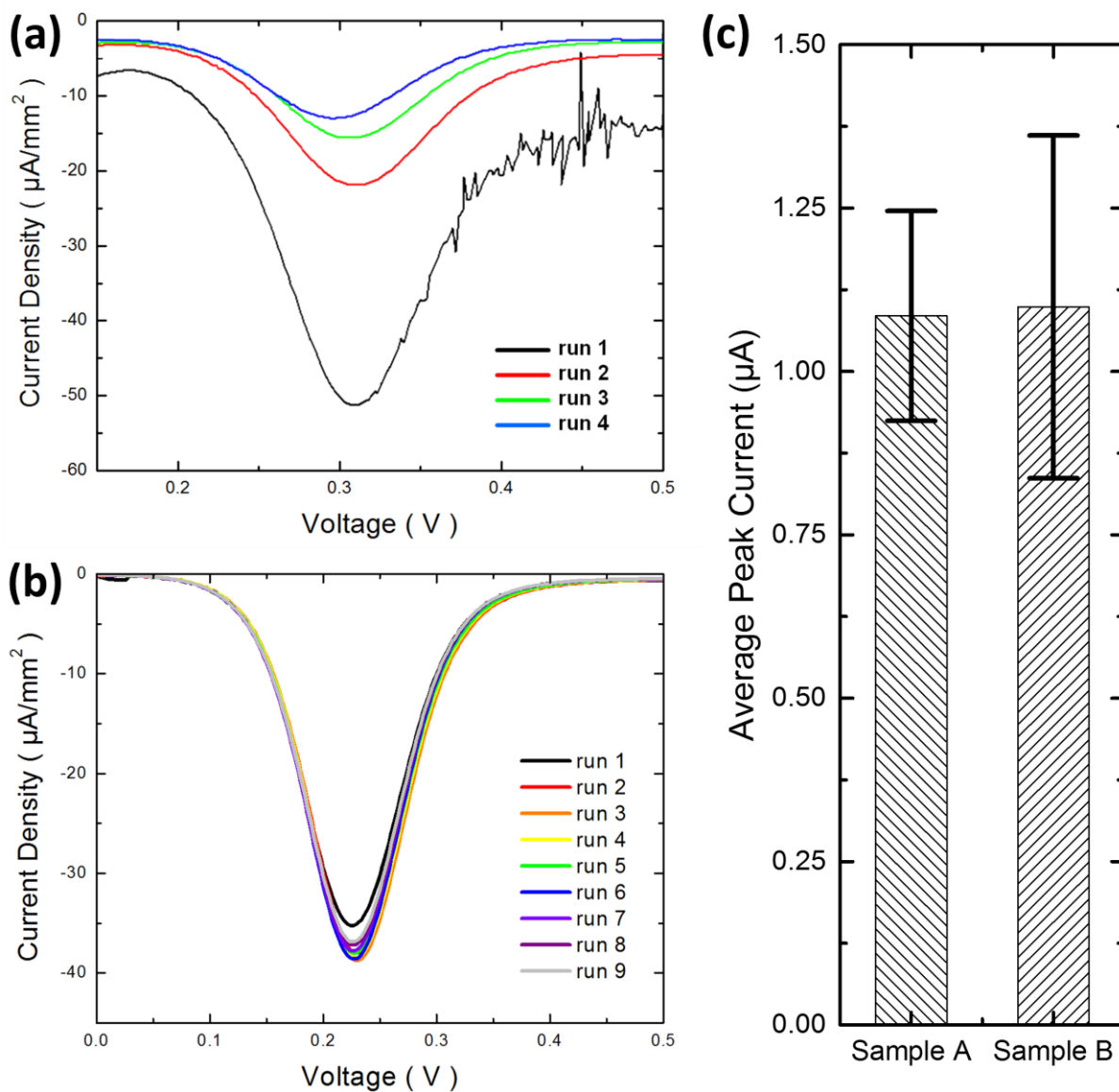
Keywords

Nanocoax, nanofabrication, extended-core, biosensor, high-sensitivity, ELISA

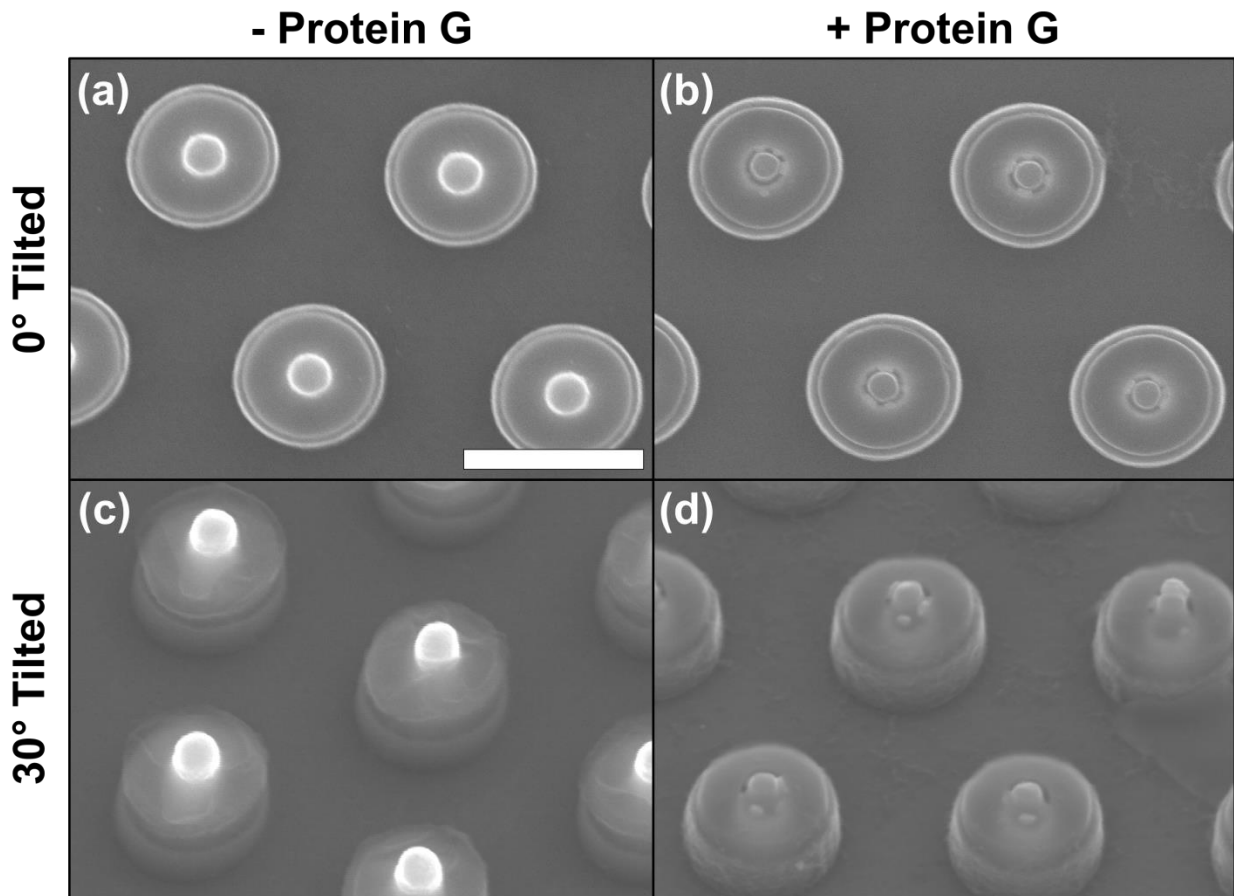
Supplementary Figures



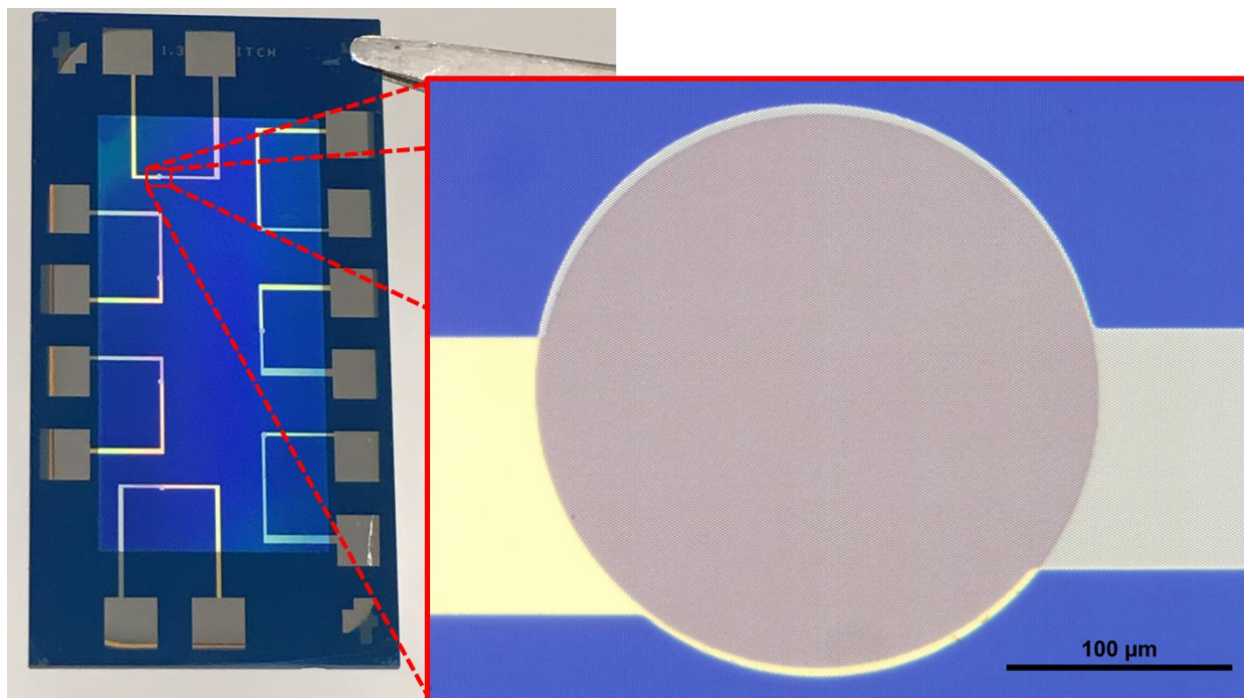
Supp. Fig. 1. Several types of Si pillar arrays were evaluated. FCA electrochemical results, in addition to the availability of chips, dictated the shape used for final testing. Slightly conical-shaped Si pillars (a) were chosen for further work. Sharp (b), cylindrical (c), and high-aspect ratio (d) pillars did not provide sufficient electrical and electrochemical consistency for further use. Scale bar inset is 1 μm for (a-c) and 2 μm for (d). SEM images taken at 30° tilt. Si substrates were imaged with a layer of Au deposited in order to reduce image distortion due to charge accumulation.



Supp. Fig. 2. Measured current density of (a) non-ECC and (b) ECC arrays for multiple repeated runs on the same region. The peak current density for non-ECC drops off quickly for subsequent runs, whereas for ECC, it shows high repeatability over 9 runs. Note the different axis ranges used. (c) Peak current and standard deviation from 6 separate sensing regions, each from independently-fabricated ECC samples.



Supp. Fig. 3. SEM images of the extended core nanocoax. SEMs of two separate arrays on the same ECC chip, (a) one incubated without protein G (- Protein G), and (b) one with protein G (+ Protein G), both prior to AuNP-conjugated antibody application. Corresponding 30° tilted views are shown in (c) and (d), respectively. AuNPs of ~40 nm diameter are visible around the extended cores of the test array (+ Protein G), but not the control array (-Protein G). Note that a particular iteration of ECC was utilized in this study, expected to be representative of the behavior of all ECC chips. Inset scale bar is 1 μ m in length.



Supp. Fig. 4. Picture of a 16 mm x 30 mm final sample with 7 separate sensing regions. Inset image is a x100 magnification of an individual sensing region, showing the leads for the inner (Au) and outer (Cr) electrodes converging to the circular nanocoax array.